ACS APPLIED MATERIALS & INTERFACES

Forum Article

www.acsami.org

Structure and Dynamics of Asymmetric Poly(styrene-*b*-1,4-isoprene) Diblock Copolymer under 1D and 2D Nanoconfinement

Wycliffe K. Kipnusu,*[,†] Mahdy M. Elmahdy,[†,‡] Emmanuel U. Mapesa,[†] Jianqi Zhang,[¶,⊥] Winfried Böhlmann,[§] Detlef-M. Smilgies,[∥] Christine M. Papadakis,[¶] and Friedrich Kremer[†]

[†]Institute of Experimental Physics I, University of Leipzig, Linnéstraße 5, 04103 Leipzig, Germany

[‡]Department of Physics, Mansoura University, Mansoura 35516, Egypt

[¶]Physik-Department, Physik weicher Materie, Technische Universität München, James-Franck-Straße 1, 85748 Garching, Germany

[§]Institute for Experimental Physics II, University of Leipzig, Linnéstraße 5, 04103 Leipzig, Germany

[∥]Cornell High Energy Synchrotron Source (CHESS), Wilson Laboratory, Cornell University, Ithaca, New York 14853, United States

Supporting Information

ABSTRACT: The impact of 1- and 2-dimensional (2D) confinement on the structure and dynamics of poly(styrene-*b*-1,4-isoprene) P(S-*b*-I) diblock copolymer is investigated by a combination of Scanning Electron Microscopy (SEM), Atomic Force Microscopy (AFM), Grazing-Incidence Small-Angle X-ray Scattering (GISAXS), and Broadband Dielectric Spectroscopy (BDS). 1D confinement is achieved by spin coating the P(S-*b*-I) to form nanometric thin films on silicon substrates, while in the 2D confinement, the copolymer is infiltrated into cylindrical anodized aluminum oxide (AAO) nanopores. After dissolving the AAO matrix having mean pore diameter of 150 nm, the SEM images of the exposed P(S-*b*-I) show straight nanorods. For the thin films, GISAXS and AFM reveal hexagonally packed cylinders of PS in a PI matrix. Three dielectrically active relaxation modes assigned to the two segmental modes of the styrene and isoprene blocks and the normal mode of the latter are studied selectively by BDS. The dynamic glass transition, related to the segmental modes of the styrene and isoprene blocks, is independent of the dimensionality and the finite sizes (down to 18 nm) of confinement, but the normal mode is influenced by both factors with 2D geometrical constraints exerting greater impact. This reflects the considerable difference in the length scales on which the two kinds of fluctuations take place.

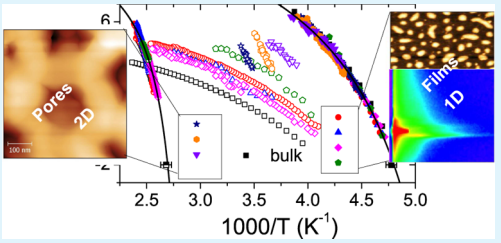

KEYWORDS: *diblock copolymers, structure, dynamics, glass transition, confinement*

1. INTRODUCTION

Structural self-assembly of block copolymers (BCPs) into ordered domains with periodicity of about 5−100 nm provides a direct means to achieve diverse nanostructures suitable for many applications such as data storage media,[1] biosensors,[2] drug delivery,[3,4] plasmonics,[5] antireflection coating,[6] nanophotonics,[7] infiltration membranes,[8] optoelectronics,[9] and nanopatterning.[4,10] In particular, the use of BCPs in nanolithography patterning is a boon to the electronic industry where the optical lithography is facing a technological and financial limit in scaling down critical dimensions of chip features to sub-22 nm.[11−13] Nanopatterning with BCPs offers a facile and low cost alternative to possibly prepare high density electronic nanoarrays with length scales down to ∼5 nm. To realize this, long-range order of the self-assembled nanodomains of BCPs is required. Electric field, solvent, and thermal annealing are currently employed to align these nanostructures[14−16] where the latter is most suitable for nanopatterning of electronic devices.[10] In this respect, the glass transition temperature T_g of the respective blocks in BCPs when confined in different dimensions is an important parameter. For instance, specific T_g's of the removable and the permanent blocks are required in order to obtain the desired nanopatterns.[10] The prospect of preparing high performing, all polymer integrated circuits[17] also increases the demand of the knowledge of how the T_g of these materials is altered at the nanoscale. Additionally, the sharp dynamic thermal annealing recently used to fabricate vertically oriented BCP thin films on an industrial scale also relies on the T_g of the respective blocks.[18] Currently, there is paucity of data on the dynamic glass transition of confined BCPs. The knowledge of the intrinsic relaxation timescale of the copolymer chains would as well be a relevant input in modeling the macroscopic ordering in BCPs.[19]

Broadband Dielectric Spectroscopy (BDS) is an ideal tool to investigate the dynamic glass transition and also the chain or normal mode relaxation in polymeric materials at the nanoscale. In BCPs, the overall dynamics also depend on the morphological changes as a consequence of nanoconfinement which is unravelled by the Grazing Incidence Small-Angle X-ray

Special Issue: Forum on Polymeric Nanostructures: Recent Advances toward Applications

Received: October 5, 2014
Accepted: February 2, 2015
Published: February 9, 2015

DOI: 10.1021/am506848s
ACS Appl. Mater. Interfaces 2015, 7, 12328−12338

Table 1. Molecular Characteristics of the P(S-*b*-I) Diblock Copolymer and Its Corresponding Homopolymers (PS and PI) Used in This Study[a]

sample	M_{nPS} (g/mol)	M_{nPI} (g/mol)	M_n (total)	M_w (total)	M_w/M_n	f_{PI}	χN at 298 K
SI-134	39800	94000	133800	139152	1.04	0.73	160.2
PI-55			52381	55000	1.05	1.0	
PS-58			58317	58900	1.01	0.0	

[a]The volume fraction of isoprene blocks f_{PI} and the Flory–Huggins interaction parameter (χ) were obtained as discussed in refs 51 and 54. M_w/M_n is the polydispersity index, and N is the degree of polymerization.

Scattering (GISAXS) technique.[20] Due to the confinement-induced reduction in entropy, interfacial interactions, symmetry breaking, and incommensurability between confining space and intrinsic domain sizes, BCPs form new self-ordered morphologies that are not present in the bulk.[9,13,21,22] In one-dimensional (1D) confinement i.e., in thin films, the ensuing morphologies are directed by the film thickness and the interfacial interactions. Depending on the preferential surface affinity of the individual blocks, parallel, perpendicular (with respect to the substrate), or even completely new structures have been achieved.[23,24] For instance, the planar substrate surface generally breaks the symmetry of the bulk cylindrical domains of BCPs inevitably adjusting their morphologies.[25−27] Because of the additional curvature effects, 2D confining geometries (e.g., in nanopores) give rise to novel structures compared to those in the bulk state.[26−31]

While a lot of experimental and theoretical efforts are geared toward understanding confinement induced morphologies of BCPs,[32−37] it is equally vital to probe the effect of the geometrical constraints on their molecular dynamics. From both technological and fundamental view points, these effects cannot be overemphasized. Molecular dynamics is therefore more emphasized in this report. For about two decades hitherto, the dynamic glass transition of confined homopolymers has been actively researched,[38−41] but similar studies on BCPs are rare. Recently, BDS was employed to probe the glassy and chain dynamics of poly(*cis*-1,4-isoprene) (PI) homopolymer confined in 1D (thin films) and in 2D (nanopores of anodic aluminum oxide AAO).[42−44] It was found that the timescale of the *segmental dynamics* is neither affected by the finite size nor by the dimensionality of confinement, while the *chain dynamics* (normal mode) is impacted by the molar mass, geometry, and size of confining space. For BCPs containing isoprene, most studies have focused on the effect of internal confinement (in the form of microdomains) on the dynamics of the isoprene blocks.[45−50] As discussed above, external hard geometrical constraints strongly influence the morphology of confined BCPs. Under similar conditions, their molecular dynamics is expected to deviate from that of the bulk state; however, this has hardly been investigated. The recent study of lamellae-forming poly(styrene-*b*-1,4-isoprene) (P(S-*b*-I)) confined in nanometric thin films revealed, to the contrary, that the timescale of segmental relaxation of the respective blocks is the same as that of the corresponding bulk homopolymers.[51] Whether these findings also hold for the asymmetric (cylindrical) P(S-*b*-I) confined in 1D and in 2D geometries remains to be proved.

As opposed to symmetric BCPs under 1D confinement, restricting cylinder-forming BCPs into nanopores leads to extreme morphological changes due to the interplay between confinement and surface curvature.[22,28,30] This is corroborated by the fact that crystallization (which strongly depends on the morphology) of BCPs confined in, for instance, AAO nanopores, is partially suppressed.[52] Most recently, Maiz et al.[53] studied dynamics of cylinder forming polystyrene-*b*-poly(4-vinylpyridine) (P(S-*b*-4VP)) in bulk and confined in AAO nanopores and found that the segmental dynamics of P4VP confined in larger pore sizes (330 nm) is slower than that of the bulk sample but becomes faster in smaller pore sizes (35 nm). Hard external confinement can therefore cause changes on the molecular dynamics of BCPs that are not easily envisaged.

In this report, Scanning Electron Microscopy (SEM), Atomic Force Microscopy (AFM), and GISAXS are employed to study the structure of asymmetric P(S-*b*-I) (isoprene volume fraction f_{PI} = 0.73) in AAO nanopores and thin films. Its molecular dynamics when confined both in 1D and 2D geometrical constraints is probed by BDS. SEM images show that P(S-*b*-I) contained in AAO pores exist as nanorods. AFM and GISAXS results reveal cylindrical structures which are oriented along the plane normal to the substrate for thicker films but mainly lie on the substrate plane for thinner films. The segmental modes of the styrene and isoprene blocks remain bulk-like regardless of the film thicknesses (d_{film} = 250−30 nm) and pore sizes (d_{pore} = 150−18 nm) utilized in this study. However, the normal mode of the isoprene blocks is influenced by both finite sizes and dimensionality of confinement.

2. EXPERIMENTAL SECTION

Materials. Poly(styrene-*block*-1,4-isoprene) P(S-*b*-I) diblock copolymer labeled SI-134 was purchased from Polymer Standards Service GmbH, while polystyrene and poly(*cis*-1,4-isoprene) homopolymers labeled PI-55 and PS-58, respectively, are products of Polymer Source, Inc. The molar masses (M_n and M_w), polydispersity indices (M_w/M_n), PI volume fractions (f_{PI}) in P(S-*b*-I), and the Flory–Huggins interaction parameter (χN) at 298 K are listed in Table 1. f_{PI} and χ were determined as described in ref 51. Silicon wafers with low resistivity (<5 mΩcm) and surface roughness (<6 Å) purchased from Microfab Service GmbH were used as substrates for thin film preparation. They have a native oxide layer of about 2 nm. Chloroform (99.9% purity), acetone (99.8% purity), and syringe filters (PTFE membrane with 0.2 μm pore size) were purchased from Sigma-Aldrich GmbH. The polymer materials and solvents were used as received without further purification. Details of the thin film preparation and the AFM measurement can be found in ref 51. The prepared films were annealed at 423 K for 24 h in high vacuum (10^{-6} mbar) before BDS measurements were carried out. AAO membranes with unidirectional nanopores used to confine P(S-*b*-I) into 2D geometries were purchased from Synkera Technologies Inc., USA. Their characteristic parameters such as the membrane thickness, porosity, average pore diameter, and density are shown in Table 2. Scanning Electron Micrographs (SEM) (as provided by the producer, Synkera) for the membrane with a mean pore diameter of 55 nm are shown in Figure S1 (Supporting Information).

Infiltration of P(S-*b*-I) into AAO Membranes. Infiltration was done by solvent vapor swelling assisted wetting of AAO nanopores.[55] A thick film in the order of 1−2 μm cast on a glass slide from a solution (20 mg/mL) of P(S-*b*-I) in chloroform was annealed at 333 K in the vacuum for 24 h. A pre-evacuated empty AAO membrane was

DOI: 10.1021/am506848s
ACS Appl. Mater. Interfaces 2015, 7, 12328−12338

Table 2. Characteristics of the Porous AAO Membranes Used in This Study

parameters	AAO-I	AAO-II	AAO-III
membrane diameter (mm)	13.0 ± 0.2	13.0 ± 0.2	13.0 ± 0.2
membrane thickness (μm)	51 ± 1	48 ± 2	50 ± 2
pore diameter (nm)	150 ± 10	55 ± 6	18 ± 3
porosity (%)	32	11	10
pore density (cm^{-2})	2×10^9	2×10^9	5×10^{10}
filling fraction (%)	50	67	87

weighed and then placed on top of the P(S-*b*-I) film in argon atmosphere. Evacuation was done by annealing the empty AAO membrane at 573 K in vacuum for 24 h. The sandwich of the P(S-*b*-I) film between a glass slide and an AAO membrane was then placed onto a Teflon spacer with the AAO membrane at the bottom as shown in Figure 1 (a). This sample setup was again annealed at 333 K in the vacuum for 6 h before the solvent (chloroform) was directly injected into the bottom of the Teflon spacer at 300 K (see Figure 1 (a)). The grooves on the bottom edge of the Teflon facilitate uniform distribution of the solvent. According to this setup, the solvent vapor enters the pores and swells/dissolves the polymer film directly above causing it to infiltrate into the pores as shown by the magnified scheme in Figure 1 (b). After 24 h, the sample setup was annealed at 373 K in a vacuum (10^{-3} mbar) for 1 h before the second injection of the solvent was done. This was repeated three times to improve the filling fraction. Excess material on the surface of the membrane was removed by wiping with a tissue soaked in chloroform. Samples were finally annealed at 423 K in vacuum (10^{-6} mbar) for 24 h and weighed thereafter. The surfaces of the empty and filled membranes are shown in Figure 1 in which (c,d) are the AFM images of the empty and filled membranes, respectively. The AFM scan of the filled membrane was taken on the bottom side surface that was not initially in contact with the P(S-*b*-I) film. As seen in Figure 1 (d), the P(S-*b*-I) infiltrated into the entire thickness of the AAO membranes. However, not all of the pores were completely filled (see the bottom left of Figure 1 d) probably due to difference in the internal surface texture. The filling fractions determined gravimetrically are shown in Table 2.

Scanning Electron Microscopy (SEM). FEI Nanolab 200 Dual Beam Microscope was used to record the SEM images of P(S-*b*-I) infiltrated into AAO nanopores. The infiltration was done as described above. After performing BDS measurement (detailed in the latter section), the same sample was used for SEM measurement. It was prepared as follows: The AAO template (with mean pore size of 150 nm) containing P(S-*b*-I) was dissolved completely in 5 wt % NaOH solution on a parafilm surface. The sample was then thoroughly rinsed with distilled water for several times before depositing it on a brass metal plate. It was finally coated with a thin gold layer of about 10 nm prior to conducting the SEM measurement. The resulting image

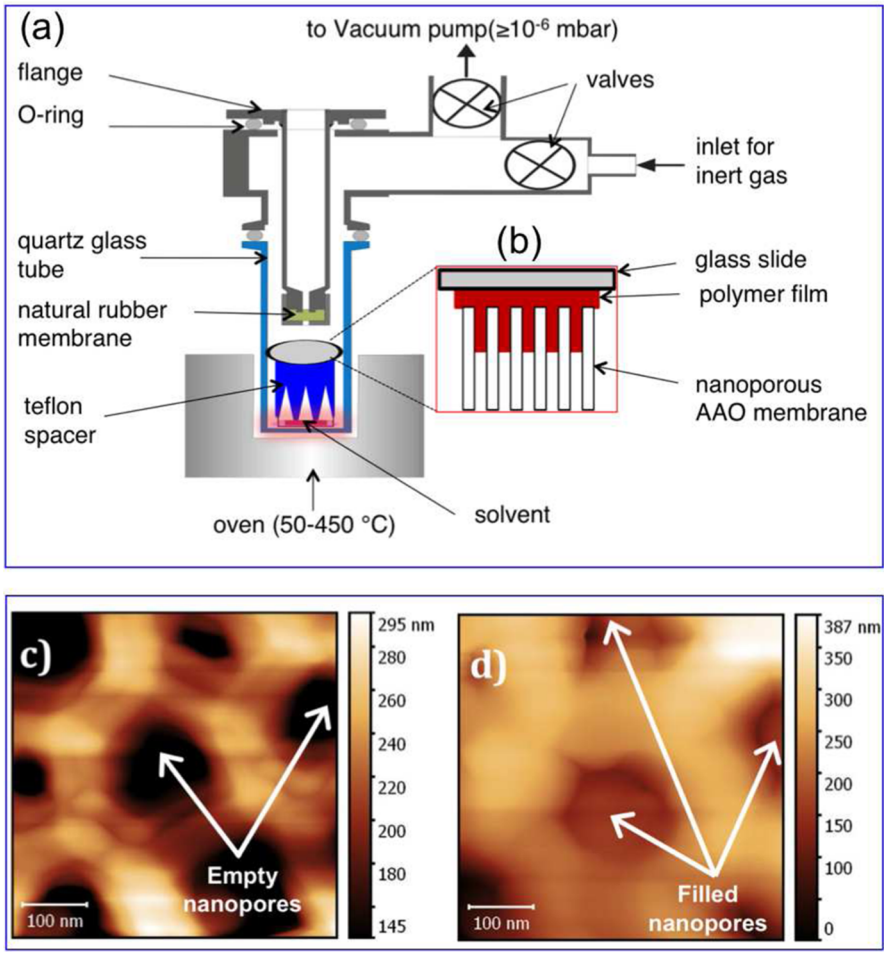

Figure 1. (a) A schematic representation of the setup used to infiltrate P(S-*b*-I) into the AAO membranes. The sample arrangement consisting of (from top to bottom) a glass-slide, P(S-*b*-I) film (about 1−2 μm), AAO membrane, and Teflon spacer (with grooves as shown) is placed in a custom-made vacuum annealing chamber. (b) A magnified scheme of this arrangement without the Teflon spacer. The sample is heated in a fused silica tube by an oven equipped with a temperature controller. Importantly, access into the vacuum (without breaking it) is gained via the natural rubber membrane using a sharp stainless needle. c) and d) shows the AFM height images (scan size 500 × 500 nm^2) of the empty and filled AAO templates (mean pore diameter = 150 nm) respectively.

DOI: 10.1021/am506848s
ACS Appl. Mater. Interfaces 2015, 7, 12328−12338

shown in Figure 2 magnified at 400× was recorded by an Everhart-Thornley Detector (ETD) at a working distance of 5.2 mm. The applied voltage was 5.0 kV.

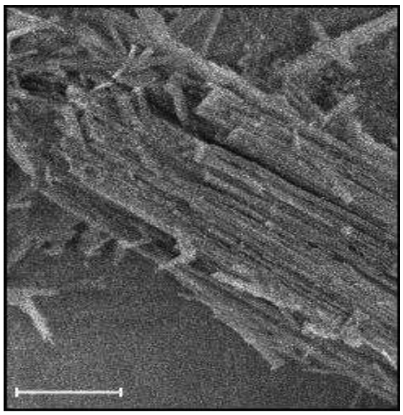

Figure 2. SEM micrograph of P(S-*b*-I) nanorods after removing AAO template which had an average pore diameter of 150 nm. Scale bar: 2 μm.

Grazing-Incidence Small-Angle X-ray Scattering (GISAXS). Scattering experiments were done at beamline D1 at the Cornell High Energy Synchrotron Source (CHESS) at Cornell University in Ithaca, NY, U.S.A. The wavelength λ was 1.16 Å with a beam size of 500 μm × 100 μm (horizontal × vertical). Scattered intensity was detected by a CCD camera having a pixel size of 46.9 μm × 46.9 μm and being placed 1.83 m from the sample resulting in a nominal q-resolution of 1.384×10^{-4} Å/pixel. q denotes the momentum transfer. The q space calibration was performed by fitting a circle to the first-order Debye–Scherrer ring of silver behenate. The conversion of the 2D images from pixels to q values as well as the construction of intensity profiles were carried out using the FIT2D program.[56] The in-plane and the normal components of the scattering vector are denoted by $q_{\|} = (q_x^2 + q_y^2)^{1/2}$ and q_z, respectively. For small incidence and scattering angles, the coordinates of the 2D detector correspond to q_y ($\approx q_{\|}$) and to q_z. The direct beam which is too intense for the detector was blocked by a blade. Similarly, the very strong specularly reflected beam that appears at an exit angle α_f equal to incident angle α_i was blocked by a rodlike beamstop. The extended wings of this peak around $q_y = 0$ can still be observed on either side of the beamstop. BCP having volume fraction of one of the blocks in the range of 0.7–0.8 mainly form hexagonally packed cylinders whose primary and higher order Bragg peaks appear at ratios of $1:\sqrt{3}:\sqrt{4}:\sqrt{7}$.[33] Out-of-plane diffuse Bragg reflections (DBRs) are observed in GISAXS images with q_y values that are quantized by the characteristic spacing (a_0) of the lattice planes oriented along the plane normal to the substrate given by

$$a_0 = \frac{2\pi}{q_y^*} \tag{1}$$

where q_y^* is the position of the first-order out-of-plane DBRs. For layered cylinders lying along the substrate plane, the DBRs appear along both q_y and q_z. Considering the DBRs along q_y, the distance of the centers of hexagonally packed cylinders is given by[58,59]

$$D = \left(\frac{2}{\sqrt{3}}\right) a_0 \tag{2}$$

From simple geometrical consideration and assuming hexagonal parking, the diameter of the cylinders can be obtained from[46]

$$d_{cyl} = 2\left(\frac{f_{PS} D^2 \sqrt{3}}{2\pi}\right)^{1/2} \tag{3}$$

where f_{PS} is the volume fraction of the styrene blocks. The radius of gyration (R_g) was estimated from the following equation:[60]

$$D = 2.7 R_g (\chi N)^{1/6} \tag{4}$$

Broadband Dielectric Spectroscopy (BDS). Dielectric measurements in the frequency (10^{-1}–10^7 Hz) and temperature (200–450 K) ranges were performed using a Novocontrol high-resolution alpha analyzer under pure nitrogen atmosphere. The sample temperatures were controlled in a nitrogen jet using a Quatro controller with stability better than 0.1 K. The sample setup for the thin film spin coated onto ultraflat silicon wafers was arranged with novel nanostructured counter electrodes.[61] An appropriate height of the nanostructures was chosen for each measurement in order to keep the upper surface of the polymer film free. For measurement of P(S-*b*-I) contained in AAO membranes, the sample was sandwiched between platinum electrodes after a thin Al foil (~800 nm) was placed on both sides of the membranes to improve the contacts. In all cases, superposition of the empirical Havriliak–Negami (HN) function including a conductivity term (eq 5) was used to fit the isothermal dielectric loss data[62]

$$\epsilon''(\omega) = \epsilon_\infty + \sum_j \frac{\Delta\epsilon_j}{[1 + (i\omega\tau_{HNj})^{\alpha_j}]^{\beta_j}} + \frac{\sigma_0}{\omega\epsilon_0} \tag{5}$$

where ϵ_∞ denotes the high frequency limit of the dielectric permittivity, $\Delta\epsilon$ is the dielectric relaxation strength, α and β are the shape parameters, and j is the index over which the relaxation processes are summed, σ_0 is the dc-conductivity, ϵ_0 is the permittivity in free space, and ω is the angular frequency ($\omega = 2\pi f$) of the external applied electric field. The relaxation at maximum loss, τ_{max}, used to generate activation plots is related to the characteristic time constant τ_{HN} by[63]

$$\tau_{max} = \tau_{HN} \sin\left(\frac{\pi\alpha\beta}{2 + 2\beta}\right)^{1/\alpha} \left(\sin\frac{\pi\alpha}{2 + 2\beta}\right)^{-1/\alpha} \tag{6}$$

The non-Arrhenius temperature dependence of τ_{max} is approximated by the Vogel–Fulcher–Tammann (VFT) equation

$$\tau_{max} = \tau_\infty \exp\left(\frac{B}{T - T_0}\right) \tag{7}$$

where τ_∞ is the high temperature limit of the relaxation time, B is the apparent activation energy, and T_0 is the "ideal" glass transition temperature or the Vogel temperature. The isochronal dielectric loss data was fitted by a temperature dependent ($\epsilon''(T)$) function (eq 8) obtained by replacing τ_{HN} in eq 5 with eq 7 assuming that $\Delta\epsilon$, α, and β are temperature invariant.

$$\epsilon''(T) = \epsilon_\infty + \sum_j \frac{\Delta\epsilon_j}{\left[1 + \left\{i\omega\tau_{\infty j} \exp\left(\frac{B_j}{T - T_{0j}}\right)\right\}^{\alpha_j}\right]^{\beta_j}} \tag{8}$$

The relaxation times (τ_{max}) of P(S-*b*-I) confined in thin films were obtained by fitting eq 5 to the data, but the dielectric loss of the sample infiltrated into AAO nanopores, except the segmental mode of PI blocks in 150 nm pores, was very weak, hence τ_{max} in this case was obtained from the isochronal data. In the frequency representation, the measured dielectric response of the polymer film in our set up includes some spurious conductivity due to the resistance of the silicon electrodes which causes an increase in the dielectric loss in the low and high frequency flanks, respectively. These artificial contributions were included in the fitting procedure and then subtracted to get the net dielectric loss of the sample (Figure S3). Similarly, for the sample in AAO nanopores, the contribution of the AAO matrix was subtracted from the measured data before fitting (Figures S4 and S5).

DOI: 10.1021/am506848s
ACS Appl. Mater. Interfaces 2015, 7, 12328–12338

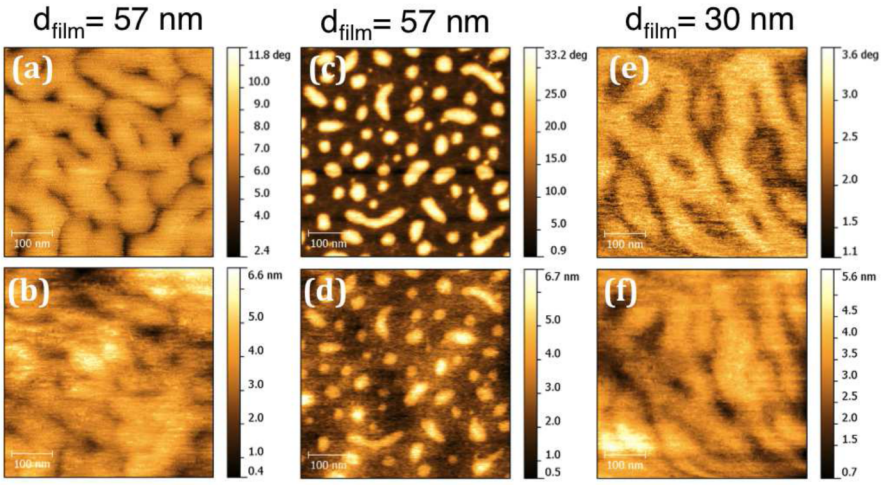

Figure 3. Tapping mode AFM images (scan size 500 × 500 nm^2) of P(S-*b*-I) films dried in an oil-free high vacuum (10^{-6} mbar) at room temperature for 24 h. The phase (a,c e) and height (b,d,f) images of the sample with film thickness 57 nm dried at room temperature (a,b), the same sample annealed at 423 K (c, d) and the sample having thickness of 30 nm annealed at 423 K.

3. RESULTS AND DISCUSSION

The Ordered State Morphology. The morphology of P(S-*b*-I) contained in the AAO matrix having mean pore sizes of 150 nm as revealed by SEM (Figure 2) shows exposed copolymer nanorods after dissolution of the confining matrix. It is therefore evident that the P(S-*b*-I) confined in this matrix formed straight nanorods as opposed to nanotubes. Such type of nanorods have also been observed by Xiang et al.[26] The SEM image of the nanorod of P(S-*b*-I) infiltrated in AAO with an average pore diameter of 18 nm appears to be twisted (or have helical shape) (Figure S2). However, the SEM images do not reveal the microphase separation, hence further investigation using Transmission Electron Microscopy (TEM) and Small Angle X-ray Scattering is required and can be reported separately.

The morphology of P(S-*b*-I) confined in thin films was investigated by AFM and GISAXS. The AFM images of the sample with d_{film} = 57 nm dried in high vacuum (10^{-6} mbar) at room temperature reveal cylindrical structures that are oriented along the substrate plane (Figure 3 a,b). After annealing this sample at 423 K, standing cylinders are observed (Figure 3 c,d). Upon decreasing the film thickness to 30 nm, the cylinders became oriented mainly along the substrate plane (Figure 3 e,f). In order to elucidate the details of the inner film structures as a function of film thickness, we performed GISAXS experiments on samples with film thicknesses of 500, 150, and 57 nm prepared under similar conditions and hence identical to the ones used in the AFM measurements. The GISAXS images taken at two incident angles, namely α_i = 0.14° and α_i = 0.08°, are shown in Figure 4. The former which is between the critical angles of total external reflection of P(S-*b*-I) (α_{cp} = 0.11°) and that of the Si substrate (α_{cs} = 0.16°) allows the X-rays to penetrate the entire film thickness, hence enabling detection of the inner film structures while the latter probes the region near the film surface because $\alpha_i < \alpha_{cp}$. The intensity in all images mostly extends along the q_y-axis. For images taken at a shallow angle of α_i = 0.08°, the intensity is low indicating that the film is homogeneous in a near-surface layer. A zoomed image of Figure 4 (e) shown in Figure 4 (g) points to the possible existence of out-of-plane DBRs at higher q_y values in addition to the first-order out-of-plane DBRs at $q_y \simeq 0.1$ nm^{-1}

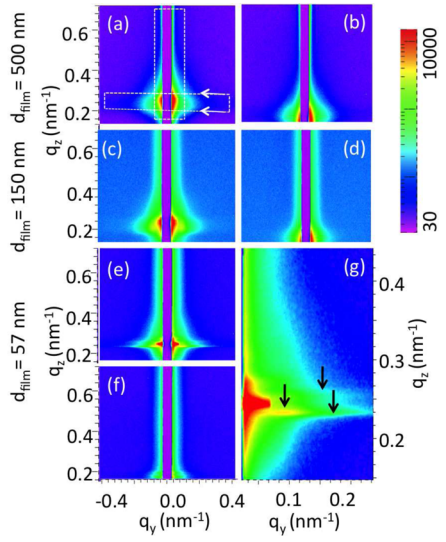

Figure 4. 2D GISAXS images for the samples having film thicknesses of 500 nm (a, b), 150 nm (c, d), and 57 nm (e, f, and g). (a, c, e, and g) represent images taken at α_i = 0.14° while (b, d, and f) were taken at α_i = 0.08°. Except (g), all the images have the same q_y and q_z scales as shown in (f). (g) is an enlargement of a section in (e) within the q_y and q_z ranges depicted in the axis. The arrows in (g) indicate the DBRs of P(S-*b*-I), while the very high intensity region is due to the specularly reflected beam. The narrow vertical rectangles are the shadows of the rod-like beam stop. The white rectangular boxes with dotted lines in (a) are the representative regions of integration used to obtain the intensity profiles along q_y and q_z, and arrows indicate the position of the Yoneda band. The intensity scale is shown on the right of (b) and (d).

as indicated by the vertical arrows. This arrangement is akin to that of standing cylinders observed by Cavicchi et al.[35]

To gain more insight, we performed integration of the images in Figure 4 (a-f) along q_y and q_z resulting in the intensity profiles plotted in the semilogarithmic scale in Figure 5. The q_y values of the first-order peaks (Figure 5a) appear at around 0.137, 0.099, and 0.101 nm^{-1} corresponding to a_0 (as given by eq 1) of 45.8, 63.4, and 62.2 nm for film thicknesses of 500, 150, and 57 nm, respectively.

DOI: 10.1021/am506848s
ACS Appl. Mater. Interfaces 2015, 7, 12328−12338

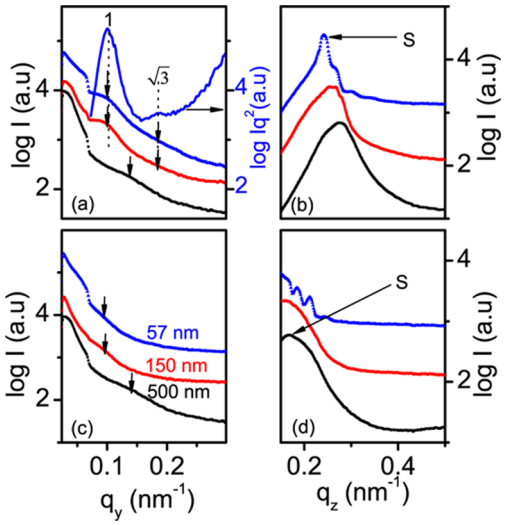

Figure 5. Intensity profiles along q_y and q_z of the 2D GISAXS images (a-f) shown in Figure 4 (a) and (b) represent profiles obtained from images taken at $\alpha_i = 0.14°$, while (c) and (d) are from images taken at $\alpha_i = 0.08°$. Only positive q_y values obtained from integration of the region shown in the 2D GISAXS images given in Figure 4. (a) In (a-d), the curves from bottom to top represent data from film thicknesses of 500, 150, and 57 as shown in (c). The upper curve in (a) is a plot of Iq^2 versus q_y, and the vertical dotted lines indicate positions of the primary and second-order Bragg peaks corresponding to the hexagonal packing of cylinders. The peaks marked S in (b) and (d) are due to the specularly reflected beam. The curves are shifted vertically for graphical reasons.

The value of a_0 for the thickest film (500 nm) is in the same range as that of the cylinder-forming P(S-*b*-I) bulk sample which is about 43 nm.[57] This film (d_{film} = 500 nm) does not show higher order Bragg peaks (Figure 5a) implying short-range ordering, but weak second-order peaks are observed for thinner films (150 and 57 nm). Just for clarity, we plot Iq^2 against q_y values for d_{film} = 57 nm (upper curve in Figure 5a). This reveals well resolved first- and second-order peaks corresponding to a ratio of 1:$\sqrt{3}$ typical for hexagonally packed standing cylinders. Intensity profiles from surface sensitive GISAXS images (Figure 5c) also show weak peaks along q_y. These peaks (the first-order peaks in Figure 5a) were used to determine the cylinder−cylinder distance (D) in the film plane based on eq 2. The diameters of the cylinders (d_{cyl}) were obtained from eq 3. The results are listed in Table 3. Considering the sample having a film thickness of 57 nm, the d_{cyl} values shown in Table 3 is in good agreement with d_{cyl} = 40.1 nm obtained from AFM (Figure 3c). The intensity

Table 3. Film Thickness (d_{film}), Cylinder−Cylinder Distance (D), the Diameters of the Cylinders (d_{cyl}), and Radius of Gyration (R_g) in the P(S-*b*-I) Diblock Copolymer[a]

d_{film} (nm)	D (nm)	D_{film}/D_0^b	d_{cyl} (nm)	R_g (nm)
bulk	49.7[b]		27.1	7.9
500	52.9	10.0	28.8	8.4
150	75.4	3.0	41.1	12.0
57	72.3	1.1	39.4	11.5

[a]The thin films values were obtained from GISAXS data for measurement done at α_i = 0.14. [b]D_0 = 49.7 nm is the cylinder−cylinder distance in the bulk determined from eq 2 with a_0 = 43 nm obtained from ref 57.

oscillations along q_z (Figure 5b,d) are probably due to the interference of the X-ray beam at the film−air and film−substrate interfaces. These become more pronounced with decreasing d_{film} and α_i.[64,65]

By combining the AFM and GISAXS results, we can conclude that samples of P(S-*b*-I) (f_{PI} = 0.73) spin-cast on silicon wafers with native oxide layer and annealed at 423 K in high vacuum (10^{-6} mbar) feature standing cylinders when the film thickness is approximately above 50 nm. Reducing the films thickness to ∼30 nm results in mainly lying cylinders, as seen in the AFM image of Figure 3 (e,f).

Dynamics. Molecular dynamics was studied by BDS which probes the relaxation of the dipolar entities in a sample. Since the T_g of PS ≃ 378 K and that of PI ≃ 200 K, their respective segmental relaxations in diblock copolymer P(S-*b*-I) are widely separated in temperature, hence assigned unambiguously. This process is related to the dynamic glass transition and is universally detected in polymer melts. In polyisoprene, an additional process (*chain dynamics*) detected at lower frequencies (higher temperatures (T)) than the *segmental dynamics* is due to the end-to-end vector fluctuations of the dipole moment along the chain contour. The dielectric loss as a function of frequency of the two processes from the isoprene blocks in P(S-*b*-I) confined in thin films is depicted in Figure 6.

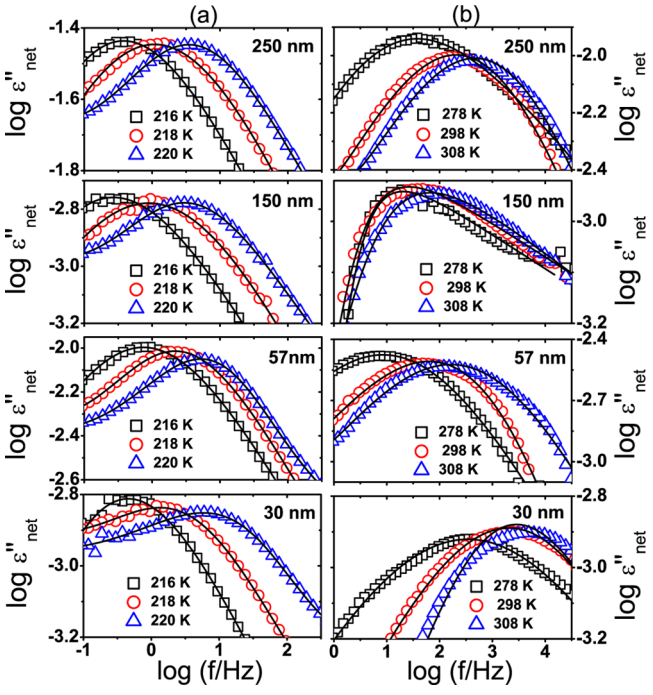

Figure 6. Isothermal dielectric loss (ϵ''_{net}) spectra for the sample with film thicknesses of 250, 150, 57, and 30 nm. (a) Segmental mode relaxation of the isoprene blocks. (b) Normal mode relaxation of the isoprene blocks at different temperatures and thickness as indicated. The solid lines in parts (a) and (b) represent the fits of eq 5.

It shows that the maximum position of the *segmental mode* is not shifted with respect to film thickness. However, this varies for the normal mode (*chain*) relaxation which becomes more apparent in the temperature dependence of τ_{max} (discussed later) obtained from HN fits as shown in Figure 6. Figure 7 shows the representative isothermal and isochronal dielectric loss data of isoprene blocks in P(S-*b*-I) constraint in AAO nanopores having a mean pore diameter of 150 nm. This

DOI: 10.1021/am506848s
ACS Appl. Mater. Interfaces 2015, 7, 12328−12338

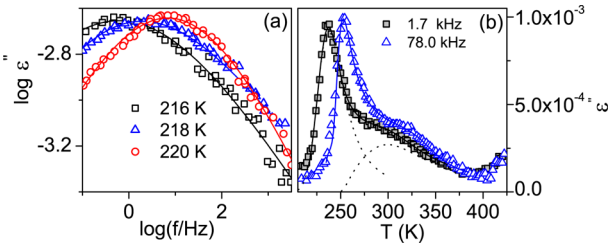

Figure 7. (a) Isothermal dielectric loss (ϵ'') of the segmental mode relaxation of the isoprene blocks confined into AAO having a mean pore diameter of 150 nm at different temperatures as indicated. (b) Corresponding plot of the isochronal representation at selected frequencies showing the segmental (low T) and normal (high T) relaxation of the isoprene blocks. The solid lines in (a) and (b) are fits according to eqs 5 and 8, respectively.

exemplifies the fitting of the data by both eqs 5 and 8. The normalized dielectric loss of these two processes for the bulk PI homopolymer and the P(S-*b*-I) confined in different film thicknesses and in AAO nanopores with average pore sizes of 150 nm is depicted in Figure 8 (a,b). The data for the *chain*

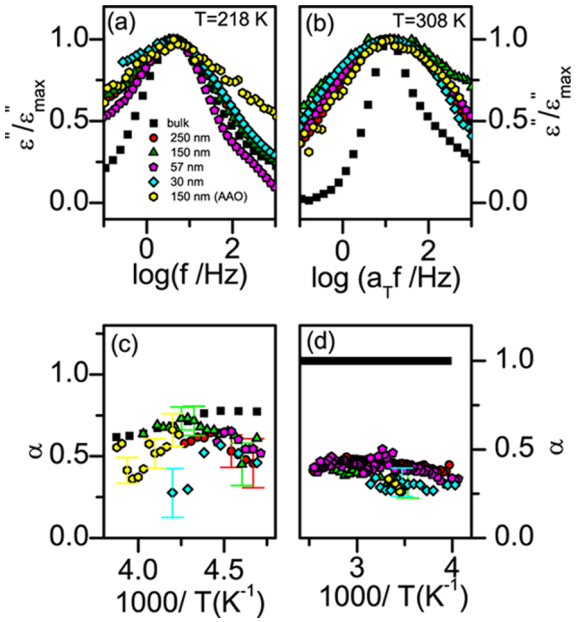

Figure 8. Comparison of the dielectric loss data normalized with respect to the maximum loss value of the segmental (a) and normal modes (b) at 218 and 308 K, respectively. The symbols for the bulk and the sample confined in thin films of different thickness and in AAO pores of 150 nm are shown in the legend of (a). The normal mode spectra shown in (b) are horizontally shifted by a factor a_T so as to coincide at the maximum of the bulk homopolymer. The HN shape parameter α obtained from eq 5 for the segmental and normal modes are shown in (c) and (d), respectively.

modes (Figure 8b) is shifted horizontally by a factor a_T but not the segmental mode (Figure 8a). The spectra (ϵ'') in Figure 8 is appreciably broadened compared to that of the bulk PI especially on the lower frequency side. This is known to exhibit a power low dependence of the form;[63] $\epsilon''(\omega) \propto \omega^{\alpha}$ where α is the HN shape parameter in eq 5. At lower temperatures, α for confined samples is systematically less than that of bulk PI (Figure 8c) confirming the observation in Figure 8(a). The global *chain dynamics*, in the bulk PI homopolymer, exhibits a true end-to-end dipole vector fluctuation (α = 1), but in the confined P(S-*b*-I), α = 0.25−0.5 implying that slower chain modes dominate since this represents broadening on the low frequency flank of the dielectric loss peak. However, this should not be construed to mean that the chain dynamics in confined P(S-*b*-I) is slower than that of bulk PI. It simply means that the relaxation time distribution is skewed to the longer times. This is caused by the highly cooperative motion of the isoprene chains due to impenetrable styrene walls. A similar finding for the case of isoprene chains confined in spherical domains of star and triblock copolymers[46,49] was attributed to the osmotic constraints (thermodynamic confinement) which arise from motion of the chains to ensure homogeneous density within the domains. Noting that broadening of segmental mode did not show up in the thin films of PI homopolymers,[42] we hereby ascribe the low frequency broadening (Figure 8a) to the osmotic constraints. The implication is that this effect takes place down to the length scale of the structural relaxation but is weak at this level to cause a shift in the mean relaxation rate of the segmental mode. The *chain dynamics* of isoprene blocks in confined P(S-*b*-I) is due to the fluctuation of free terminal subchains which can easily be affected by topological constraints and their interactions with the substrate and the domain interfaces. This explains the greater difference between the data for bulk PI and confined isoprene blocks in P(S-*b*-I) shown in Figure 8 (b,d). Due to a larger surface area in AAO nanopores, the chain−substrate interaction increases causing adsorption of some chains on the pore walls hence leading to increased broadening of $\epsilon''(\omega)$.

For further comparison of the effect of dimensionality of confinement, we show in Figure 9, the isochronal dielectric loss

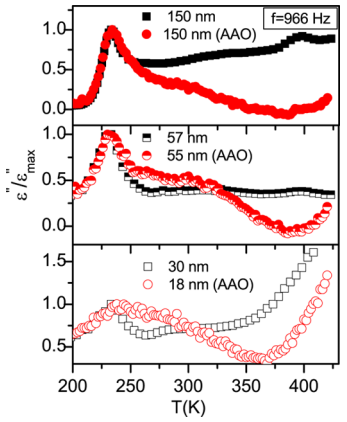

Figure 9. Comparison of the isochronal dielectric loss spectra of the P(S-*b*-I) sample in thin films (squares) and in AAO nanopores (circles) obtained at 966 Hz. The data is normalized with respect to the maximum loss value of the segmental mode of the isoprene blocks.

of P(S-*b*-I) confined in 1D and in 2D geometries with $d_{film} \approx d_{pore}$. The data is normalized with respect to ϵ''_{max} of the segmental mode of the isoprene blocks. In this representation, all the three dielectrically active modes in P(S-*b*-I) are observed. The peaks of the segmental modes of isoprene (lower T) and styrene blocks (higher T) are separated by the isoprene chain modes. The segmental mode of the styrene blocks for the film thickness of 30 nm and pore sizes of 55 and 18 nm is masked by the strong conductivity contribution. Both the segmental and the chain modes are greatly broadened for the sample in AAO nanopores with d_{pore} = 18 nm compared to the one

DOI: 10.1021/am506848s
ACS Appl. Mater. Interfaces 2015, 7, 12328−12338

confined in thin films with d_{film} = 30 nm which is ascribed to increased adsorption effect. This effect of chain adsorption causing broadening of $\epsilon''(\omega)$ with respect to AAO pore sizes for the case of unentangled PI homopolymer is discussed in detail by Alexandris et al.[43] Similar studies of chain dynamics of PI confined in controlled porous glasses (CPG) with a mean pore diameter of 10.2 nm shows a pronounced broadening that increases with the increase in the end-to-end distance of the chains.[66]

Due to weak dielectric loss of P(S-*b*-I) confined in AAO especially in smaller pores, and the nontrivial sample geometry in thin films, analysis of dielectric strengths would be prone to large uncertainties, and hence we mainly discuss the dynamics. An activation plot (Figure 10) gives a summary of the effect of

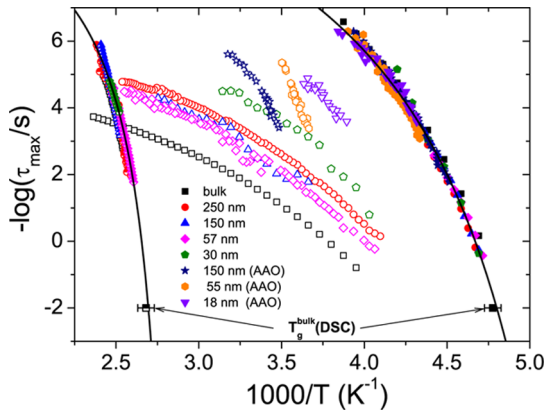

Figure 10. Activation plot of the relaxation rates corresponding to the segmental mode of the isoprene blocks (filled symbols), normal mode of the isoprene blocks (open symbols), and segmental mode of the styrene blocks (half-filled symbols) for the sample in the bulk state, and when confined in thin films and in AAO nanopores with film thickness and pore sizes as indicated in the legend. Bulk PI and PS-homopolymers with M_w = 55000 (PI-55) and 58900 (PS-58) gram/mol, respectively, are included for comparison (squares). The bulk T_g values of PI and PS determined by DSC at a scanning rate of 10 K/min are also shown. The solid lines are VFT fits to the experimental data (eq 7). The fit parameters $\tau_\infty = 2.4 \times 10^{-10}$ s, B = 243 K, and T_0 = 355 K for the styrene block, while they are 3.9×10^{-13} s, 516, and 170 K, respectively, for the isoprene block.

1D and 2D geometrical constraints on the overall molecular dynamics of P(S-*b*-I). The relaxation rates obtained from the fits of eqs 5 and 8 to the isothermal $\epsilon''(\omega)$ and isochronal $\epsilon''(T)$ data, respectively, are plotted as a function of inverse temperature. It is observed that all the data from different film thicknesses and pore sizes for the segmental/structural relaxation of either styrene (higher T) or isoprene blocks (lower T) collapse to a single curve regardless of the dimensionality and the finite-sizes of confining geometries utilized in this study. This data follows the VFT type of thermal activation. The lines in Figure 10 represent the fit of the data by the VFT eq 7.

Phenomenologically, T_g is defined as the temperature at which τ = 100 s. The T_g obtained from this definition for the styrene and isoprene blocks coincides, within experimental accuracy, with that of bulk homopolymers determined calorimetrically. Confinement of asymmetric P(S-*b*-I) in 1D (d_{film} = 250−30 nm) and in 2D (d_{pore} = 150−18 nm) has no impact on the T_g of the respective blocks. This is consistent with the finding that the glass transition takes place at the length scale of about 0.5−1 nm.[61,67]

However, the *chain dynamics* of isoprene blocks under 1D and 2D confinement is faster than that of the bulk PI (Figure 10). It is even faster when confined in 2D constraints compared to 1D, and it increases with decreasing d_{pore}. Nonetheless, the relaxation rate of this mode changes nonmonotonically in 1D confinement where it decreases with d_{film} up to ∼57 nm below which (d_{film} = 30 nm) it becomes faster than in d_{film} = 250 nm by about 1 order of magnitude. This corresponds to a change in the degree of confinement (expressed by the ratio: d_{film}/D_0^b, shown in Table 3) of about 50%. Since this is the fluctuation of the free chains, it is likely to be affected by the confinement induced morphological changes in P(S-*b*-I) e.g. radius of gyration, intercylinder distance (listed in Table 3), their orientations, and interaction with the substrate. Therefore, besides confinement, interface effects are paramount. The confinement-induced configurational changes of P(S-*b*-I) restricted in AAO nanopores can be quantified by the ratio, d_{pore}/D_0^b where D_0^b is the cylinder spacing in the bulk sample. Using this relationship, we obtained the ratios 3.0, 1.1, and 0.4 for pore sizes of 150, 55, and 18 nm, respectively. This corresponds to concentric (150 nm) and helical structures (55 and 18 nm) of P(S-*b*-I) located in AAO as predicted by simulations[30] and also evident in Figure S2. These conformational changes can cause deviations in the *chain dynamics* with respect to bulk, but another important parameter is the chain adsorption which can effectively reduce the end-to-end distance of the free terminal subchains resulting to faster relaxation. The packing of helical structures in smaller pores would also allow for more free volume leading to faster *chain dynamics* compared to concentric cylinders in larger pores.

In thin films, the packing density of the chains can be quantified by the radius of gyration obtained from eq 4. As shown in Table 3, R_g increases by ∼40% with the reduction in d_{film} from 500−57 nm implying that the chains are more stretched in thinner films hence increasing their interaction with the substrate. These interactions can change appreciably if the orientation of the cylinders with respect to substrate change, for instance from standing to lying position. According to Pickett's Model[68] for equilibrium orientation of symmetric diblock copolymers, higher density of free-chains at the substrate interface increases the fraction of lamellae that are oriented along the substrate plane. Similar scenario is expected to prevail for cylinder forming BCPs.[69] Consequently, the adsorption of part of these chains (isoprene blocks, in this case) on the substrate reduces the end-to-end vector leading to faster normal mode fluctuations.[42,70] This explains the observation that the *chain dynamics* in thinner films ∼30 nm exhibiting lying cylinders (Figure 3 e,f) is faster by about 1 order of magnitude.

4. CONCLUSIONS

The morphology of asymmetric P(S-*b*-I) BCP, f_{PI} = 0.73 confined in AAO templates and in thin films have been investigated by a combination of SEM, AFM, and GISAXS. The morphology in larger pores (150 nm) consists of continuous nanorods as revealed by SEM. For the thin films, the results from AFM and GISAXS show that the sample forms hexagonally packed cylinders which are predominantly oriented along the plane normal to the substrate for thicker films (500−57 nm) but changes to mainly parallel to the substrate plane when the thickness decreases to 30 nm. Molecular dynamics under 1D (thin films) and 2D (nanopores) geometrical

DOI: 10.1021/am506848s
ACS Appl. Mater. Interfaces 2015, 7, 12328−12338

constraints has been studied by BDS. The segmental relaxation of isoprene and styrene blocks and the *chain dynamics* due to fluctuation of the end-to-end vector in isoprene blocks are observed. The segmental mode of both blocks which is related to the dynamic glass transition is neither affected by the finite-sizes nor the dimensionality of confinement. Their T_gs therefore remain bulk-like and identical to that of the corresponding homopolymers. However, the *chain dynamics* of the isoprene blocks is affected by both the size and dimensionality of confinement. This is attributed to the osmotic constraints and the interaction of the chains with the substrate which also causes broadening of the relaxation processes.

■ ASSOCIATED CONTENT

Ⓢ Supporting Information

SEM micrographs of empty AAO membranes having a mean pore diameter of 55 nm and the one with 18 nm (pore sizes) filled with P(S-*b*-I) and partially dissolved in 5% NaOH. Details of the analysis of the BDS data to get the net response of P(S-*b*-I) confined in AAO pores and in thin films are also shown. This material is available free of charge via the Internet at http://pubs.acs.org.

■ AUTHOR INFORMATION

Corresponding Author

*E-mail: kipnusu@physik.uni-leipzig.de.

Present Address

[⊥]National Center for Nanoscience and Technology (NCNST), No. 11 Zhong Guan Cun Bei Yi Tiao, 100190 Beijing, P.R. China.

Notes

The authors declare no competing financial interest.

■ ACKNOWLEDGMENTS

Financial support by SFB/TRR 102 within the project "Polymers under multiple constraints: restricted and controlled molecular order and mobility" and the support by the NSF & NIH/NIGMS via NSF award DMR-0936384 for the CHESS facility are gratefully acknowledged. J.Z. and C.M.P. thank Deutsche Forschungsgemeinschaft (Pa771/10-1) for funding. We thank Prof. Dr. Pablo D. Esquinazi for availing the SEM equipment.

■ REFERENCES

(1) Ross, C. Pattern Magnetic Recording Media. *Annu. Rev. Mater. Res.* **2001**, *31*, 203−235.

(2) Shin, D. O.; Jeong, J.-R.; Han, T. H.; Koo, C. M.; Park, H.-J.; Lim, Y. T.; Kim, S. O. A Plasmonic Biosensor Array by Block Copolymer Lithography. *J. Mater. Chem.* **2010**, *20*, 7241−7247.

(3) Rösler, A.; Vandermeulen, G. W. M.; Klok, H.-A. Advanced Drug Delivery Devices via Self-assembly of Amphiphilic Block Copolymers. *Adv. Drug Delivery Rev.* **2012**, *64*, 270−279.

(4) Schacher, F. H.; Rupar, P. A.; Manners, I. Functional Block Copolymers: Nanostructured Materials with Emerging Applications. *Angew. Chem., Int. Ed.* **2012**, *51*, 7898−7921.

(5) Mistark, P. A.; Park, S.; Yalcin, S. E.; Lee, D. H.; Yavuzcetin, O.; Tuominen, M. T.; Russell, T. P.; Achermann, M. Block-Copolymer-Based Plasmonic Nanostructures. *ACS Nano* **2009**, *3*, 3987−3992.

(6) Joo, W.; Kim, Y.; Jang, S.; Kim, J. K. Antireflection Coating with Enhanced Anti-scratch Property from Nanoporous Block Copolymer Template. *Thin Solid Films* **2011**, *519*, 3804−3808.

(7) Lim, H. S.; Lee, J.-H.; Walish, J. J.; Thomas, E. L. Dynamic Swelling of Tunable Full-Color Block Copolymer Photonic Gels via Counterion Exchange. *ACS Nano* **2012**, *6*, 8933−8939.

(8) Phillip, W. A.; O'Neill, B.; Rodwogin, M.; Hillmyer, M. A.; Cussler, E. L. Self-Assembled Block Copolymer Thin Films as Water Filtration Membranes. *ACS Appl. Mater. Interfaces* **2010**, *2*, 847−853.

(9) Segalman, R. A.; McCulloch, B.; Kirmayer, S.; Urban, J. J. Block Copolymers for Organic Optoelectronics. *Macromolecules* **2009**, *42*, 9205−9216.

(10) Black, C.; Ruiz, R.; Breyta, G.; Cheng, J.; Colburn, M.; Guarini, K.; Kim, H.-C.; Zhang, Y. Polymer Self Assembly in Semiconductor Microelectronics. *IBM J. Res. Dev.* **2007**, *51*, 605−633.

(11) Ito, T.; Okazaki, S. Pushing the Limits of Lithography. *Nature* **2000**, *406*, 1027−1031.

(12) Ruiz, R.; Kang, H.; Detcheverry, F. A.; Dobisz, E.; Kercher, D. S.; Albrecht, T. R.; de Pablo, J. J.; Nealey, P. F. Density Multiplication and Improved Lithography by Directed Block Copolymer Assembly. *Science* **2008**, *321*, 936−939.

(13) Kim, H.-C.; Park, S.-M.; Hinsberg, W. D. Block Copolymer Based Nanostructures: Materials, Processes, and Applications to Electronics. *Chem. Rev.* **2010**, *110*, 146−177.

(14) Marencic, A. P.; Register, R. A. Controlling Order in Block Copolymer Thin Films for Nanopatterning Applications. *Annu. Rev. Chem. Biomol. Eng.* **2010**, *1*, 277−297.

(15) Zhang, J.; Posselt, D.; Sepe, A.; Shen, X.; Perlich, J.; Smilgies, D.-M.; Papadakis, C. M. Structural Evolution of Perpendicular Lamellae in Diblock Copolymer Thin Films during Solvent Vapor Treatment Investigated by Grazing-Incidence Small-Angle X-Ray Scattering. *Macromol. Rapid Commun.* **2013**, *34*, 1289−1295.

(16) Ferrarese Lupi, F.; Giammaria, T. J.; Seguini, G.; Vita, F.; Francescangeli, O.; Sparnacci, K.; Antonioli, D.; Gianotti, V.; Laus, M.; Perego, M. Fine Tuning of Lithographic Masks through Thin Films of PS-b-PMMA with Different Molar Mass by Rapid Thermal Processing. *ACS Appl. Mater. Interfaces* **2014**, *6*, 7180−7188.

(17) Drury, C. J.; Mutsaers, C. M. J.; Hart, C. M.; Matters, M.; de Leeuw, D. M. Low-cost all-Polymer Integrated Circuits. *Appl. Phys. Lett.* **1998**, *73*, 108−110.

(18) Singh, G.; Batra, S.; Zhang, R.; Yuan, H.; Yager, K. G.; Cakmak, M.; Berry, B.; Karim, A. Large-Scale Roll-to-Roll Fabrication of Vertically Oriented Block Copolymer Thin Films. *ACS Nano* **2013**, *7*, 5291−5299.

(19) Horvat, A.; Knoll, A.; Krausch, G.; Tsarkova, L.; Lyakhova, K. S.; Sevink, G. J. A.; Zvelindovsky, A. V.; Magerle, R. Time Evolution of Surface Relief Structures in Thin Block Copolymer Films. *Macromolecules* **2007**, *40*, 6930−6939.

(20) Müller-Buschbaum, P. Grazing Incidence Small-Angle X-ray Scattering: an Advanced Scattering Technique for the Investigation of Nanostructured Polymer Films. *Anal. Bioanal. Chem.* **2003**, *376*, 3−10.

(21) Lazzari, M.; Lòpez-Quintela, M. Block Copolymers as a Tool for Nanomaterial Fabrication. *Adv. Mater.* **2003**, *15*, 1583−1594.

(22) Shi, A.-C.; Li, B. Self-assembly of Diblock Copolymers under Confinement. *Soft Matter* **2013**, *9*, 1398−1413.

(23) Lyakhova, K. S.; Sevink, G. J. A.; Zvelindovsky, A. V.; Horvat, A.; Magerle, R. Role of Dissimilar Interfaces in Thin Films of Cylinder-forming Block Copolymers. *J. Chem. Phys.* **2004**, *120*, 1127−1137.

(24) Albert, J. N.; Epps, T. H., III Self-Assembly of Block Copolymer Thin Films. *Mater. Today* **2010**, *13*, 24−33.

(25) Knoll, A.; Horvat, A.; Lyakhova, K. S.; Krausch, G.; Sevink, G. J. A.; Zvelindovsky, A. V.; Magerle, R. Phase Behavior in Thin Films of Cylinder-Forming Block Copolymers. *Phys. Rev. Lett.* **2002**, *89*, 035501.

(26) Xiang, H.; Shin, K.; Kim, T.; Moon, S. I.; McCarthy, T. J.; Russell, T. P. Block Copolymers under Cylindrical Confinement. *Macromolecules* **2004**, *37*, 5660−5664.

(27) Sevink, G. J. A.; Zvelindovsky, A. V. A. Block Copolymers Confined in a Nanopore: Pathfinding in a Curving and Frustrating Flatland. *J. Chem. Phys.* **2008**, *128*, 084901.

(28) Shin, K.; Xiang, H.; Moon, S. I.; Kim, T.; McCarthy, T. J.; Russell, T. P. Curving and Frustrating Flatland. *Science* **2004**, *306*, 76.

DOI: 10.1021/am506848s
ACS Appl. Mater. Interfaces 2015, 7, 12328−12338

(29) Feng, J.; Liu, H.; Hu, Y. Mesophase Separation of Diblock Copolymer Confined in a Cylindrical Tube Studied by Dissipative Particle Dynamics. *Macromol. Theory Simul.* **2006**, *15*, 674−685.
(30) Yu, B.; Sun, P.; Chen, T.; Jin, Q.; Ding, D.; Li, B.; Shi, A.-C. Confinement-Induced Novel Morphologies of Block Copolymers. *Phys. Rev. Lett.* **2006**, *96*, 138306.
(31) Chen, P.; Liang, H.; Shi, A.-C. Origin of Microstructures from Confined Asymmetric Diblock Copolymers. *Macromolecules* **2007**, *40*, 7329−7335.
(32) Huinink, H.; Brokken-Zijp, J.; Van Dijk, M.; Sevink, G. J. A. Asymmetric Block Copolymers Confined in a Thin Film. *J. Chem. Phys.* **2000**, *112*, 2452.
(33) Tsarkova, L.; Knoll, A.; Krausch, G.; Magerle, R. Substrate-Induced Phase Transitions in Thin Films of Cylinder-Forming Diblock Copolymer Melts. *Macromolecules* **2006**, *39*, 3608−3615.
(34) Knoll, A.; Tsarkova, L.; Krausch, G. Nanoscaling of Microdomain Spacings in Thin Films of Cylinder-Forming Block Copolymers. *Nano Lett.* **2007**, *7*, 843−846.
(35) Cavicchi, K. A.; Russell, T. P. Solvent Annealed Thin Films of Asymmetric PolyisoprenePolylactide Diblock Copolymers. *Macromolecules* **2007**, *40*, 1181−1186.
(36) Shin, C.; Ryu, D. Y.; Huh, J.; Kim, J. H.; Kim, K.-W. Order-to-Order Transitions of Block Copolymer in Film Geometry. *Macromolecules* **2009**, *42*, 2157−2160.
(37) Gu, X.; Gunkel, I.; Hexemer, A.; Gu, W.; Russell, T. P. An In Situ Grazing Incidence X-Ray Scattering Study of Block Copolymer Thin Films During Solvent Vapor Annealing. *Adv. Mater.* **2014**, *26*, 273−281.
(38) Wallace, W. E.; van Zanten, J. H.; Wu, W. L. Influence of an Impenetrable Interface on a Polymer Glass-transition Temperature. *Phys. Rev. E* **1995**, *52*, R3329−R3332.
(39) Schönhals, A.; Goering, H.; Schick, C.; Frick, B.; Zorn, R. Glassy Dynamics of Polymers Confined to Nanoporous Glasses Revealed by Relaxational and Scattering Experiments. *Eur. Phys. J. E* **2003**, *12*, 173−178.
(40) Zhang, C.; Guo, Y.; Priestley, R. D. Glass Transition Temperature of Polymer Nanoparticles under Soft and Hard Confinement. *Macromolecules* **2011**, *44*, 4001−4006.
(41) Kremer, F. *Dynamics in Geometrical Confinement*; Advances in Dielectrics; Springer: London, 2014.
(42) Mapesa, E. U.; Tress, M.; Schulz, G.; Huth, H.; Schick, C.; Reiche, M.; Kremer, F. Segmental and Chain Dynamics in Nanometric Layers of poly(cis-1,4-isoprene) as Studied by Broadband Dielectric Spectroscopy and Temperature-modulated Calorimetry. *Soft Matter* **2013**, *9*, 10592−10598.
(43) Alexandris, S.; Sakellariou, G.; Steinhart, M.; Floudas, G. Dynamics of Unentangled cis-1,4-Polyisoprene Confined to Nanoporous Alumina. *Macromolecules* **2014**, *47*, 3895−3900.
(44) Mapesa, E. U.; Popp, L.; Kipnusu, W. K.; Tress, M.; Kremer, F. Molecular Dynamics in 1- and 2-D Confinement as Studied for the Case of Poly(Cis-1,4-Isoprene). *Soft Mater.* **2014**, *12*, S22−S30.
(45) Yao, M. L.; Watanabe, H.; Adachi, K.; Kotaka, T. Dielectric Relaxation Behavior of Styrene-isoprene Diblock Copolymers: Bulk Systems. *Macromolecules* **1991**, *24*, 2955−2962.
(46) Floudas, G.; Paraskeva, S.; Hadjichristidis, N.; Fytas, G.; Chu, B.; Semenov, A. N. Dynamics of Polyisoprene in Star Block Copolymers Confined in Microstructures: A Dielectric Spectroscopy Study. *J. Chem. Phys.* **1997**, *107*, 5502−5509.
(47) Willner, L.; Lund, R.; Monkenbusch, M.; Holderer, O.; Colmenero, J.; Richter, D. Polymer Dynamics under Soft Confinement in a Self-assembled System. *Soft Matter* **2010**, *6*, 1559−1570.
(48) Matsumiya, Y.; Chen, Q.; Uno, A.; Watanabe, H.; Takano, A.; Matsuoka, K.; Matsushita, Y. Dielectric Behavior of Styrene−Isoprene (SI) Diblock and SIIS Triblock Copolymers: Global Dynamics of I Blocks in Spherical and Cylindrical Domains Embedded in Glassy S Matrix. *Macromolecules* **2012**, *45*, 7050−7060.
(49) Chen, Q.; Matsumiya, Y.; Iwamoto, T.; Nishida, K.; Kanaya, T.; Watanabe, H.; Takano, A.; Matsuoka, K.; Matsushita, Y. Dielectric Behavior of Guest cis-Polyisoprene Confined in Spherical Microdomain of Triblock Copolymer. *Macromolecules* **2012**, *45*, 2809−2819.
(50) Lund, R.; Barroso-Bujans, F.; Slimani, M. Z.; Moreno, A. J.; Willner, L.; Richter, D.; Alegra, A.; Colmenero, J. End-to-End Vector Dynamics of Nonentangled Polymers in Lamellar Block Copolymer Melts: The Role of Junction Point Motion. *Macromolecules* **2013**, *46*, 7477−7487.
(51) Kipnusu, W. K.; Elmahdy, M. M.; Tress, M.; Fuchs, M.; Mapesa, E. U.; Smilgies, D.-M.; Zhang, J.; Papadakis, C. M.; Kremer, F. Molecular Order and Dynamics of Nanometric Thin Layers of Poly(styrene-b-1,4-isoprene) Diblock Copolymers. *Macromolecules* **2013**, *46*, 9729−9737.
(52) Michell, R. M.; Blaszczyk-Lezak, I.; Mijangos, C.; Müller, A. J. Confinement Effects on Polymer Crystallization: From Droplets to Alumina Nanopores. *Polymer* **2013**, *54*, 4059−4077.
(53) Maiz, J.; Zhao, W.; Gu, Y.; Lawrence, J.; Arbe, A.; Alegra, A.; Emrick, T.; Colmenero, J.; Russell, T. P.; Mijangos, C. Dynamic Study of Polystyrene-block-Poly(4-vinylpyridine) Copolymer in Bulk and Confined in Cylindrical Nanopores. *Polymer* **2014**, *55*, 4057−4066.
(54) Khandpur, A. K.; Foerster, S.; Bates, F. S.; Hamley, I. W.; Ryan, A. J.; Bras, W.; Almdal, K.; Mortensen, K. Polyisoprene-Polystyrene Diblock Copolymer Phase Diagram near the Order-Disorder Transition. *Macromolecules* **1995**, *28*, 8796−8806.
(55) Mei, S.; Feng, X.; Jin, Z. Polymer Nano Fibers by Controllable Infiltration of Vapour Swollen Polymers into Cylindrical Nanopores. *Soft Matter* **2013**, *9*, 945−951.
(56) Andy, H. The FIT2D homepage:http://www.esrf.eu/computing/scientific/FIT2D/ (accessed Feb 1, 2015).
(57) Dyer, C.; Driva, P.; Sides, S. W.; Sumpter, B. G.; Mays, J. W.; Chen, J.; Kumar, R.; Goswami, M.; Dadmun, M. D. Effect of Macromolecular Architecture on the Morphology of Polystyrene−Polyisoprene Block Copolymers. *Macromolecules* **2013**, *46*, 2023−2031.
(58) Lecommandoux, S.; Borsali, R.; Schappacher, M.; Deffieux, A.; Narayanan, T.; Rochas, C. Microphase Separation of Linear and Cyclic Block Copolymers Poly(styrene-b-isoprene): SAXS Experiments. *Macromolecules* **2004**, *37*, 1843−1848.
(59) Papadakis, C.; Darko, C.; Di, Z.; Troll, K.; Metwalli, E.; Timmann, A.; Reiter, G.; Förster, S. Surface-induced Breakout Crystallization in Cylinder-forming P(I-b-EO) Diblock Copolymer Thin Films. *Eur. Phys. J. E* **2011**, *34*, 1292−8941.
(60) Hernández, N.; Benson, C.; Cochran, E. W. Thermodynamics of Symmetric Diblock Copolymers Containing Poly(styrene-ran-styrene-sulfonic acid). *Macromolecules* **2013**, *46*, 179−187.
(61) Tress, M.; Mapesa, E. U.; Kossack, W.; Kipnusu, W. K.; Reiche, M.; Kremer, F. Glassy Dynamics in Condensed Isolated Polymer Chains. *Science* **2013**, *341*, 1371−1373.
(62) Havriliak, S.; Negami, S. A Complex Plane Representation of Dielectric and Mechanical Relaxation Processes in some Polymers. *Polymer* **1967**, *8*, 161−210.
(63) Kremer, F.; Schönhals, A. *Broadband Dielectric Spectroscopy*; Springer: Berlin, 2003.
(64) Müller-Buschbaum, P.; Stamm, M. Correlated Roughness, Long-Range Correlations, and Dewetting of Thin Polymer Films. *Macromolecules* **1998**, *31*, 3686−3692.
(65) Sun, Y.-S.; Chien, S.-W.; Wu, P.-J. Effects of Film Instability on Roughness Correlation and Nanodomain Ordering in Ultrathin Films of Asymmetric Block Copolymers. *Macromolecules* **2010**, *43*, 5016−5023.
(66) Petychakis, L.; Floudas, G.; Fleischer, G. Chain Dynamics of Polyisoprene Confined in Porous Media. A Dielectric Spectroscopy Study. *Europhys. Lett.* **1997**, *40*, 685−690.
(67) Berthier, L.; Biroli, G.; Bouchaud, J.-P.; Cipelletti, L.; Masri, D. E.; L'Hôte, D.; Ladieu, F.; Pierno, M. Direct Experimental Evidence of a Growing Length Scale Accompanying the Glass Transition. *Science* **2005**, *310*, 1797−1800.
(68) Pickett, G. T.; Witten, T. A.; Nagel, S. R. Equilibrium surface orientation of lamellae. *Macromolecules* **1993**, *26*, 3194−3199.

DOI: 10.1021/am506848s
ACS Appl. Mater. Interfaces 2015, 7, 12328−12338

(69) Kriksin, Y. A.; Khalatur, P. G.; Neratova, I. V.; Khokhlov, A. R.; Tsarkova, L. A. Directed Assembly of Block Copolymers by Sparsely Patterned Substrates. *J. Phys. Chem. C* **2011**, *115*, 25185−25200.
(70) Meins, T.; Dingenouts, N.; Kübel, J.; Wilhelm, M. In Situ Rheodielectric, ex Situ 2D-SAXS, and Fourier Transform Rheology Investigations of the Shear-Induced Alignment of Poly(styrene-b-1,4-isoprene) Diblock Copolymer Melts. *Macromolecules* **2012**, *45*, 7206−7219.

DOI: 10.1021/am506848s
ACS Appl. Mater. Interfaces 2015, 7, 12328−12338